

3D PRINTING

Critical instability at moving keyhole tip generates porosity in laser melting

Cang Zhao^{1,2*}, Niranjan D. Parab^{3†}, Xuxiao Li⁴, Kamel Fezzaa³, Wenda Tan⁴, Anthony D. Rollett^{5,6*}, Tao Sun^{7*}

Laser powder bed fusion is a dominant metal 3D printing technology. However, porosity defects remain a challenge for fatigue-sensitive applications. Some porosity is associated with deep and narrow vapor depressions called keyholes, which occur under high-power, low-scan speed laser melting conditions. High-speed x-ray imaging enables operando observation of the detailed formation process of pores in Ti-6Al-4V caused by a critical instability at the keyhole tip. We found that the boundary of the keyhole porosity regime in power-velocity space is sharp and smooth, varying only slightly between the bare plate and powder bed. The critical keyhole instability generates acoustic waves in the melt pool that provide additional yet vital driving force for the pores near the keyhole tip to move away from the keyhole and become trapped as defects.

Laser powder bed fusion (LPBF), currently the most extensively used metal additive manufacturing process, is revolutionizing the manufacturing industry (1–3). In a typical LPBF process, a high-power-density laser is scanned across a thin powder layer, under the guidance of a digital computer-aided design and drafting (CADD) model, to locally melt the metal powder and fuse it to the previous layer. Despite LPBF's unrivaled capability for directly fabricating parts with complex geometries, the associated porosity remains its Achilles heel because it impairs the performance—for example, corrosion resistance and fatigue life—of the product (4). Intensive research efforts have advanced the understanding and control of the porosity (5). Of the various mechanisms that cause porosity, the keyhole mode of melting has recently attracted broad attention because of its importance in laser welding (6) and most especially in LPBF, as revealed with high-speed synchrotron x-ray imaging (7).

In keyhole-mode melting, the strong recoil pressure from the rapid evaporation of metal pushes the surrounding melt liquid downward, creating a deep and narrow cavity called a keyhole. Inside the keyhole, the laser beam undergoes multiple reflections, which largely enhances laser absorption and improves energy efficiency (7–10). However, under some

laser conditions, the keyhole walls constantly fluctuate and collapse. This process is generally attributed to the complex interplays among the thermocapillary force, Marangoni convection, recoil pressure, and appearance of gas plasma (11–13). Such keyhole instability generates pores, which become detrimental structural defects in the build if trapped by the solidification front.

Power-velocity (P - V) mapping (14–16), which directly relates product quality (density or porosity) to the process parameters (sometimes with hatch spacing), is an effective but heuristic tool for LPBF users. One of the missing pieces in the physical foundation of P - V maps is whether the so-called “keyhole porosity boundary,” which separates processing conditions that produce nominally fully dense parts from those with pores, is well defined and reproducible. Moreover, in LPBF, the presence of powder has been linked to larger keyhole fluctuations and greater pore formation when compared with those of laser melting of bare plate (7). However, quantification of the boundary and any powder-induced shift is lacking. The relevant spatiotemporal scales of keyhole pore formation require subnanosecond temporal resolution, micrometer spatial resolution, and megahertz frame rates. These are precisely the domain of synchrotron x-ray imaging, allowing us to investigate keyhole pore formation.

We used operando high-speed x-ray imaging at a third-generation high-energy light source (17–21) for the completion of this missing piece in the P - V map by quantitatively outlining the keyhole porosity boundary, elucidating the powder effect, and revealing the fundamental origin of keyhole pores and their initial motions during the LPBF process. The sample was a thin Ti-6Al-4V plate (~400 μm in thickness) (fig. S1A) with, for certain experiments, a layer of powder on top and sandwiched together between two glassy carbon plates. A

laser beam with a Gaussian profile and in continuous wave mode scanned the sample along a single straight line at various powers (P) and speeds (V). Meanwhile, we recorded full-field x-ray images at high spatial (2.0 to 3.0 $\mu\text{m}/\text{pixel}$) and temporal (0.1 to 7500 ns) resolutions at high frame rates (50 to 5000 kHz) (22).

The keyhole porosity boundary separating the keyhole porosity regime from the stable melting regime was unexpectedly smooth and sharp, with or without the presence of powder (Fig. 1A). Across the boundary toward higher energy density, discernable pores were released into the liquid from the keyhole bottom (Fig. 1B). The maximum pore size (among all observed in any given experiment) trended up with decreasing scan speed at a constant laser power. A few cases deviated from this trend, most likely because of variations in powder bed thickness in different samples and from the short time window available for x-ray imaging relative to the pore-formation events. With decreasing laser power, the keyhole porosity boundary becomes increasingly sensitive to scan speed, particularly in the presence of powder, and appeared to asymptote to a threshold in power.

Pore formation, regardless of laser power and the presence or absence of powder, occurred when the bottom tip of a letter “J”-shaped keyhole was pinched off, released at high speed toward the wake of the laser beam, and eventually trapped by the solidification front (Fig. 1B and figs. S3, A, C, and D, and S4). This process suggests a dominant mechanism for keyhole pore formation around the boundary, in which acoustic waves push the pinched-off pore(s) away from the keyhole. Meanwhile, the “role of powder” region, bounded by the two boundaries (with and without powder) (Fig. 1A), joins two subregions. In the high-power-velocity (high- PV) region, for a constant scan speed, lower power was needed for a powder bed sample to generate keyhole pores, whereas in the low-power-velocity (low- PV) region, higher power was needed. This interesting result implies a secondary keyhole pore formation mechanism (fig. S3, B and E). Near the low- PV boundary, the large and rapid fluctuation of a dramatically narrowed straight keyhole of high aspect ratio induces small pores directly beneath the laser beam, which resembles the stationary laser melting situation when the laser beam is turned off or shaded (17, 23). This area in the P - V space also largely overlaps with the transition zone we defined (7), in which the keyhole is prone to fluctuate in the depth direction. Compared with bare plate samples, in which such pores tend to merge quickly into the subsequent growing keyhole and disappear, the larger keyhole fluctuations in powder bed samples create sufficient waiting time for the pores. These pores are nearly stationary after pinching off the keyhole and

¹Department of Mechanical Engineering, Tsinghua University, Beijing 100084, China. ²Key Laboratory for Advanced Materials Processing Technology, Ministry of Education, Beijing 100084, China. ³X-ray Science Division, Argonne National Laboratory, Lemont, IL 60439, USA. ⁴Department of Mechanical Engineering, University of Utah, Salt Lake City, UT 84112, USA. ⁵Department of Materials Science and Engineering, Carnegie Mellon University, Pittsburgh, PA 15213, USA. ⁶NextManufacturing Center, Carnegie Mellon University, Pittsburgh, PA 15213, USA. ⁷Department of Materials Science and Engineering, University of Virginia, Charlottesville, VA 22904, USA.

*Corresponding author. Email: cangzhao@tsinghua.edu.cn (C.Z.); rollett@andrew.cmu.edu (A.D.R.); ts7qw@virginia.edu (T.S.)

†Present address: Intel Corporation, 2501 NE Century Boulevard, Hillsboro, OR 97124, USA.

suspended inside the melt pool (or potentially accelerated by the local melt flow through forces such as drag away from the keyhole) (22) to be pinned by the advancing solidification front.

The keyhole porosity boundary is closely related to the keyhole depth, d_1 (and the melt pool depth, d_m) (fig. S2B). Typically, at a constant laser power, keyhole pores form only when the keyhole depth is larger than a threshold, d_c (fig. S6, A and G). This threshold increases, statistically, with scan speed (Fig. 2A) and laser power (Fig. 2B) in distinct power-law forms, $d_c \sim V^6$ and $d_c \sim P$, respectively. In general, the relationships between the keyhole depth (d_1) away from the boundary and the two processing parameters (P and V) are complicated and highly coupled, $d_1 \sim (AP + B)/V$ ($A > 0$ and $B < 0$ are constants) (figs. S5 to S7) (22). The smooth and sharp keyhole porosity boundary may imply that the condition for keyhole pore formation is material-constant-dependent or keyhole-geometry-dependent. An examination of the keyhole depth threshold (Fig. 2G) reveals a simple linear relationship with the energy density (E) in the high- PV segment, $d_c \sim E$, with the slope being the same with or without powder (50 cm³/MJ) and the difference between their vertical intercepts being ~ 100 μm (close to the powder bed thickness).

However, this linearity in the $d_c \sim E$ plot does not hold for the data in the low- PV range. An energy density threshold $E_c \sim 3.7$ MJ/m² appears, below which no keyhole pores form. This also implies the secondary mechanism for the keyhole pore formation in this region, which we attributed to the keyhole depth fluctuations.

The relative fluctuation R (the coefficient of variation of keyhole depth) increased strongly with decreasing scan speed and laser power in the low- PV range of the keyhole porosity boundary (Fig. 2, D and E). Especially in the presence of powder, $R > 1$. This means that the laser sometimes drills very deep, far beyond the average and across the sustainable depth, and leaves a pore at the keyhole bottom (movie S7). Additionally, the powder-induced relative fluctuation ΔR_p (the difference between presence versus absence of powder) changed dramatically with the laser condition (Fig. 2E, inset). This indicates that the powder motion has substantial influence on the keyhole pore generation. We speculate that powder particles occasionally enter the laser beam and shade the keyhole momentarily from full direct laser illumination before flying away (24). This abruptly but temporarily lowers the local temperature on the surface layer of the keyhole walls and the recoil pressure on the liquid below the surface layer and thereby promotes the keyhole depth fluctuation. Our observations (Fig. 2, C and F) collectively confirm the intrinsic connection between keyhole depth

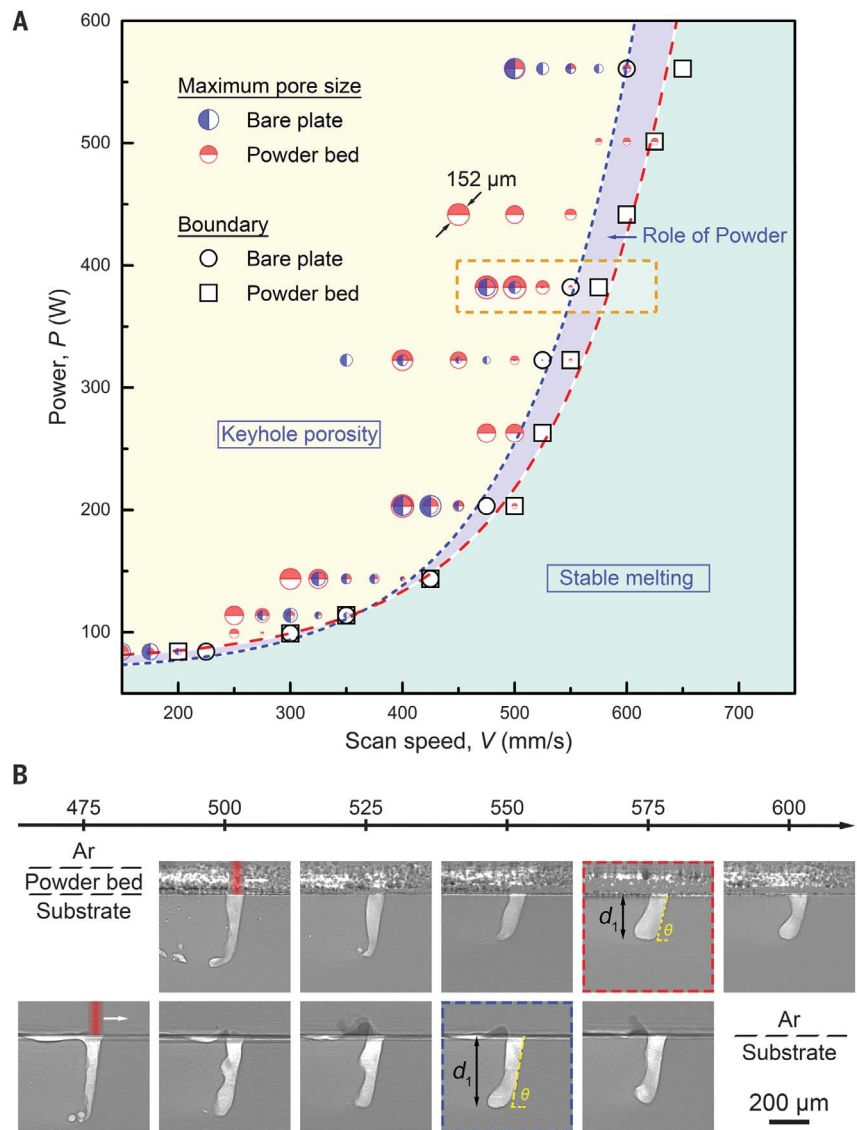


Fig. 1. Keyhole porosity boundary and role of powder in laser melting. (A) P - V space, which is divided into a stable melting regime (light green shaded area, consisting of stable keyhole, transition, and conduction regimes) and a keyhole porosity regime (light yellow area), indicated by open circles and a blue short-dashed line for the case of bare plate and by open squares and a red long-dashed line for samples with a ~ 105 - μm powder layer on top. The extent to which adding powder increases the instability and widens the porosity regime is indicated by the light purple shaded regions and a blue arrow identifying the role of powder. In the keyhole porosity regime, the diameters of the blue and red half solid circles indicate the measured maximum equivalent pore size for each specific P - V combination. The dashed lines are to guide the eye. (B) Tableau of representative x-ray images at constant $P = 382$ W and varying scan speed across the keyhole porosity boundary indicated by the orange dashed rectangle in (A). (Top) Powder bed samples. (Bottom) Bare plate samples. The red and blue dashed framed images correspond to the respective boundaries in scan speed, below which pores are trapped in the resolidified metal. The overall keyhole depth, d_1 , and front keyhole wall angle, θ , are labeled. All images were background corrected by the images collected before laser melting. The laser spot size is ~ 100 μm .

and keyhole porosity and complements the keyhole porosity boundary in the P - V space (Fig. 1A).

During a laser scan, most of the incident beam impinges on the front keyhole wall (8,9). In the stable keyhole regime, the projection of

the front keyhole wall on the sample surface is the effective laser spot D_0 . In previous studies, D_0 was constant across the P - V space, regressed from the nearly linear d_1 versus $\tan\theta$ relationship, where θ is the front keyhole wall angle (6,7). This, however, fails when the

P - V combination crosses the keyhole porosity boundary (Fig. 2H). As the laser scan speed decreased, the projected length of the front keyhole wall s (defined as $d_f/\tan\theta$, along the laser scan direction) fluctuated at first around D_0 and then decreased with V . Two possible reasons could explain this trend. The Gaussian

profile of the laser concentrates the intensity at the center, and the edge of the beam at low power does not provide sufficient energy to vaporize the metal. The low scan speed tends to increase the front keyhole wall angle (beyond a threshold called Brewster's angle), largely reducing the laser absorption of the

low-power Gaussian beam and further cutting off the edge of the front keyhole wall (22).

The depth-to-length aspect ratio of a keyhole appears to be a good indicator for the keyhole pore formation (Fig. 1B) as well as the maximum keyhole pore size (Fig. 1A). Regardless of the broadening of the keyhole

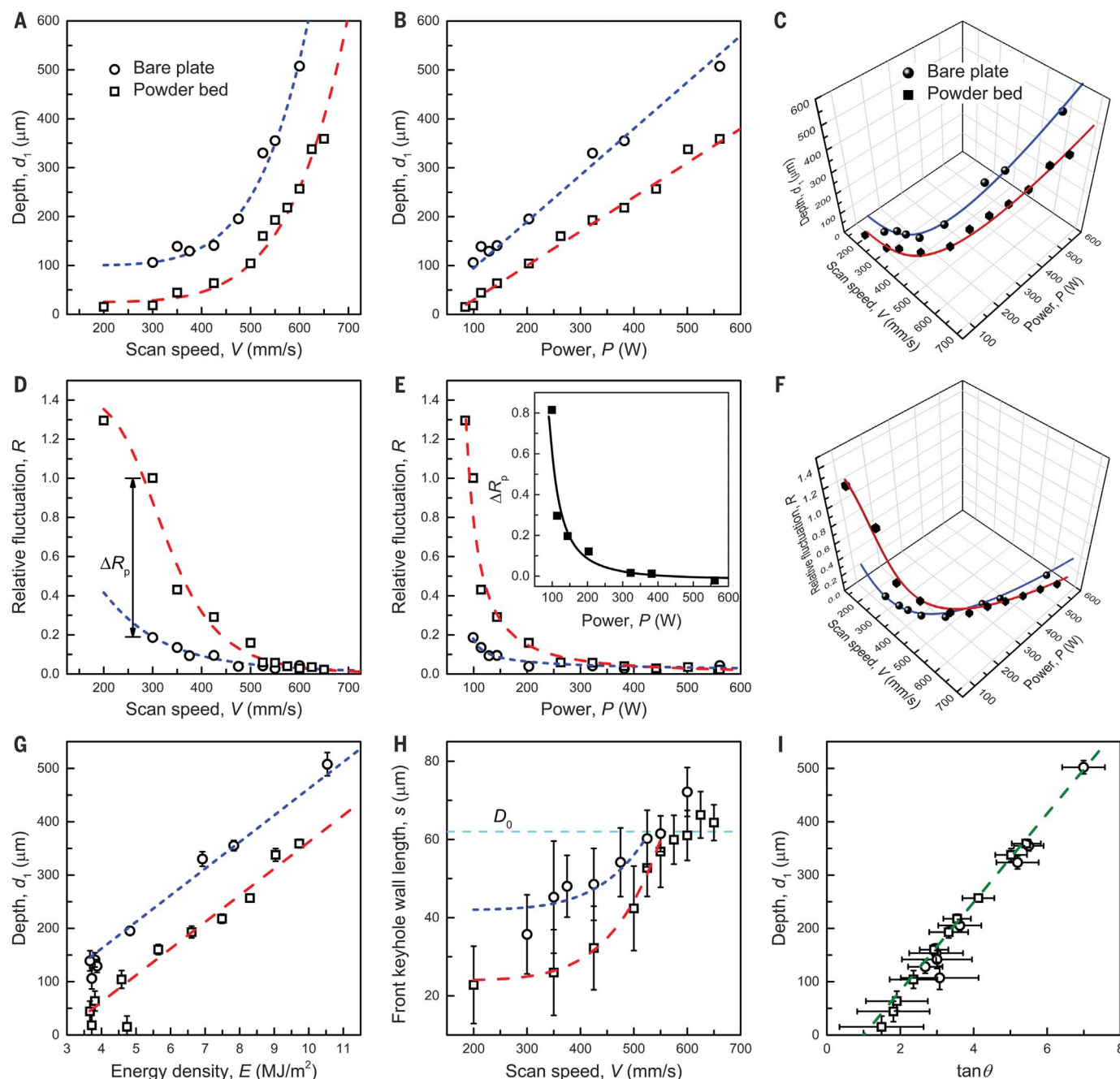


Fig. 2. Keyhole scaling and fluctuation on the porosity boundary. (A and B) Keyhole depth, d_f , as a function of (A) scan speed V and (B) laser power P . (C) Keyhole depth in the P - V space. (D and E) Relative fluctuation of keyhole depth, $R = \Delta d_f/d_f$, as a function of (D) scan speed and (E) laser power. (F) Relative fluctuation of keyhole depth in the P - V space. (G) Keyhole depth as a function of energy density E . (H) Front keyhole wall length, s , as a function of scan speed. The

length is defined as $d_f/\tan\theta$, where θ is the front keyhole wall angle. The horizontal dashed line indicates the effective laser spot size D_0 in the stable keyhole regime. (I) Keyhole depth as a function of tangent of front keyhole wall angle. The green dashed line in (I) is linearly regressed through all data points. The circles with blue lines are from bare plate samples, and the squares with red lines are powder bed samples. The error bar of each datum point represents the standard deviation.

by multiple reflections and Fresnel absorption (fig. S7E), the tangent of front keyhole wall angle is closely related to the aspect ratio (fig. S7F). On the keyhole porosity boundary, the keyhole depth threshold clearly follows a linear relationship with $\tan\theta$ (Fig. 2I). Data from both bare plate and powder bed samples fall on the same line as $d_c = \alpha(\tan\theta - 1)$, where α is $\sim 83\ \mu\text{m}$, which is evidently larger than the effective laser spot D_0 ($\sim 62\ \mu\text{m}$). We call α the keyhole pore constant. Another characteristic of our plot is that the horizontal intercept of the line is around $\tan\theta = 1$, which suggests that keyhole pores are only generated when the keyhole depth is larger than its length on the boundary. The linearity in the relationship (Fig. 2, B and I) is well maintained over the entire keyhole porosity boundary, despite that the mechanisms for generating a pore at high- and low- PV segments could be different. This suggests a deep connection between the dominant and secondary mechanisms.

A dominant mechanism exists for pore formation near the keyhole porosity boundary in which instability forms pores and acoustic waves drive them away from the keyhole tip, regardless of laser power and the presence or absence of powder. We used megahertz x-ray imaging to measure the keyhole and pore evolutions with high spatial and temporal resolutions (Fig. 3A; figs. S8, S13, S17, and S19; and movies S11 and S12). In general, four phases of the process can be defined: (i) formation of a mini-keyhole, (ii) formation of an instant keyhole pore (P_0), (iii) formation of a needle-like keyhole bottom (NKB), and (iv) rapid pore motion away from the keyhole and pinning.

The sequence of events leading to the formation of a keyhole pore starts from a letter “J”-shaped keyhole and a mini-keyhole on top of a protrusion on the front keyhole rim (Fig. 3A) (9, 25). The mini-keyhole creates a strong recoil on the side surface of the protrusion, driving it to swing down and impact on the rim of the rear keyhole wall. During this process, the keyhole wall underneath the protrusion, particularly the region close to the front wall, receives much-reduced laser energy. This results in a drop of the local recoil pressure, the subsequent rapid liquid filling driven by the surface tension (9, 26), and eventually, the impact of the liquid on the side surface of the rear wall. The collapse of this keyhole region occurred at a horizontal speed of $\sim 13\ \text{m/s}$ (fig. S9) (22), giving rise to a “newborn” keyhole, a pore P_0 , and a high-speed microjet (fig. S10).

Pore P_0 then undergoes an asymmetric collapse (Fig. 3, B to D and F, and figs. S8 and S10). In the first few microseconds after pore P_0 pinches off the keyhole, the original keyhole tip is almost stationary. This phenomenon occurs because the high overheating on the free side of the surface layer (approximately hundreds of kelvin above the boiling

point) and the limited thermal diffusion of the heat toward the surrounding liquid (a few micrometers in a few microseconds) maintain the pressure balance through continuous vaporization for a short period. By contrast, the top-right edge of pore P_0 moves very fast, driven by the rapidly piercing microjet (Fig. 3D and figs. S10 and S15C). When the microjet tip P_{jet} impinges on the opposite wall of the pore, the impact speed is $\sim 16\ \text{m/s}$, and we estimated the “water hammer” pressure (27, 28) to be $\sim 140\ \text{MPa}$ (22). This process results in rapid pore collapse, splitting, and rebound (Fig. 3F, fig. S11, and movie S11) and an acoustic wave (29, 30). This impact mechanism is analogous to the shock wave-pore interaction in liquids by laser or ultrasound (29, 31).

Unlike the overall keyhole depth d_1 , the mini- and newborn keyhole depth d_2 surprisingly exhibited a repetitive pattern (Fig. 3E). The process begins from a protrusion on the front keyhole rim, grows to the overall keyhole depth, and ends with the creation of a successor keyhole. With the keyhole collapse time t_1 being the reference, the shifted keyhole depth had a global drill rate of $\sim 17\ \text{m/s}$ before entering the plateau stage (fig. S15A), which allowed us to estimate the average temperature of the melt at the keyhole bottom as $3900\ \text{K}$ (22).

Despite this creation process, the keyhole pore survives only under a certain set of conditions. A protrusion structure may exist at the bottom of the front keyhole wall (for example, Fig. 3A, time $8.28\ \mu\text{s}$, and fig. S14, $47.84\ \mu\text{s}$), which caused the reduction of the recoil pressure applied to the liquid beneath the keyhole tip surface. This keyhole tip was reshaped into a narrow NKB (for example, Fig. 3J, time $9.20\ \mu\text{s}$, and Fig. 3K, $48.76\ \mu\text{s}$) by the acoustic wave induced by the pore rebound, with facilitation by the surface tension effect (Fig. 3H). We found evidence of this from the directional reshaping, mainly on the side facing the pore (Fig. 3K), and from the nearly synchronized response of the NKB to the pore. Because of these two aforementioned effects, the newborn keyhole depth d_2 experiences a rapid drop at t_2 (Fig. 3E). The NKB emits another strong acoustic wave (Fig. 3I), driving the pore to migrate away, before which the pore is almost stationary (for example, Fig. 3J, pore P_1).

A keyhole with a needle-shaped bottom is unstable. So once the protrusion disappears (Fig. 3J and fig. S12) or the laser drills through (Fig. 3K and fig. S14), the keyhole can then focus the laser intensity inside the NKB through multiple reflections (fig. S15D) (22), creating the conditions for rapid drilling and keyhole expansion. An acoustic wave was generated after the formation of the NKB, as shown by the almost instantaneous and synchronized responses of pores P_1 and P_2 (Fig. 3I and movie S11); the pore P_1 was accelerated from nearly stationary to $\sim 10\ \text{m/s}$ in less than $1\ \mu\text{s}$ and then

decelerated (fig. S16); and the initial deformation and even collapse of the pore was largely on the side facing the NKB. We found traces of microjet penetration, whereas the far side was unperturbed (Fig. 3, J and K, and figs. S11 and S14).

We speculate that the explosive behavior of the NKB was due to phase explosion. This defines an extreme material behavior caused by rapid heating; when the local temperature approaches the critical point, a metastable liquid decomposes instantly into a mixture of gas and fine droplets (32–34). In addition to the strongly enhanced laser absorption on the NKB walls, several observations support this idea (Fig. 3, J and K, and figs. S12, S14, and S22). (i) The keyhole bottom expansion starts roughly from the inside of the NKB, for which we found evidence from features around the center of the expanded bottom. (ii) The expanding keyhole walls were roughened and wrinkled, which suggested an impact by the gas-droplet mixture. (iii) The primary pore may collapse first, before the expansion (not widening). The explosion of the surface-layer liquid at the keyhole bottom emits an acoustic wave directly into the liquid below, which travels at the sound speed (C). The wave amplitude was indicated by the rapid pore collapse (for example, through microjetting), with the collapse speed of $\sim 18\ \text{m/s}$ (Fig. 3K and fig. S14) and the water hammer pressure of $\sim 150\ \text{MPa}$ (22). In the wake of the wave, the liquid pressure dropped, causing a sudden widening of the keyhole bottom (Fig. 3K, time $49.68\ \mu\text{s}$, and fig. S14).

Limited by the short interaction time ($D_p/C \sim$ a few nanoseconds, where D_p is the equivalent pore diameter), the pore can gain sufficient kinetic energy and escape from the large thermal gradient field around the keyhole only when the amplitude of the acoustic wave from the NKB is high enough. The amplitude appears higher along the depth direction because the pores tend to migrate downward first. In addition to the acoustic wave and the inertial force of the liquid jet it causes (35), the translational motion of a pore around the keyhole bottom is collectively controlled by the thermocapillary force (36) and the viscous drag force (35). These are determined by the local thermal gradient and the Marangoni flow, respectively. The thermocapillary force always attracts the pore to the keyhole, whereas the viscous drag force, because the local melt tends to flow away from the keyhole, does so only when the pore moves faster than the local melt along the same direction. This confirms the importance of the acoustic wave in porosity formation in combination with keyhole instability [more discussion is provided in (22), Generation and role of acoustic waves].

With insufficient kinetic energy from the acoustic wave, the pore remains in the region

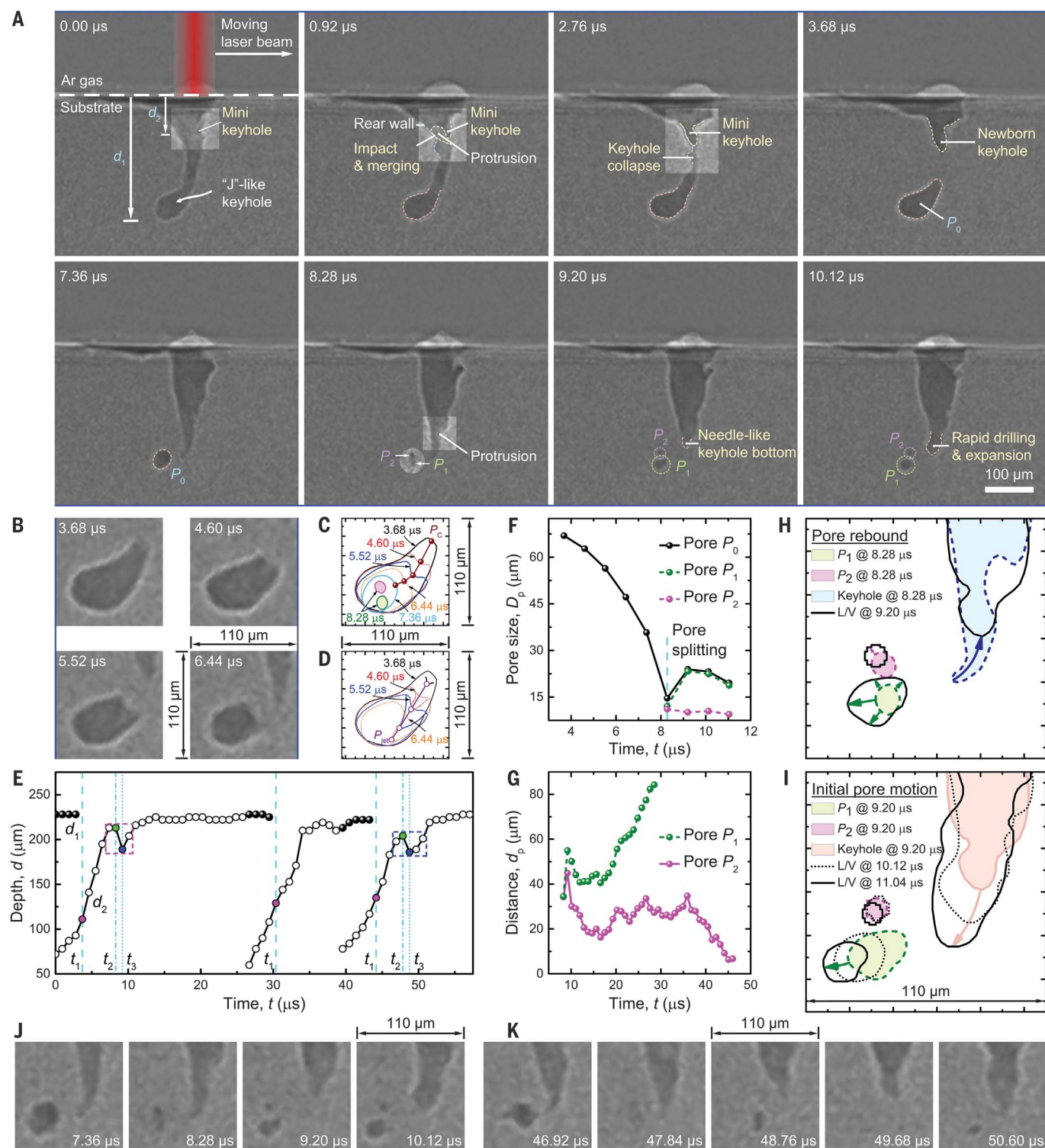


Fig. 3. Keyhole pore formation and motion driven by acoustic waves from keyhole instability. (A) Megahertz x-ray images of a keyhole pore-formation process. (B) X-ray images showing the nonuniform collapse of pore P_0 , driven by a microjet. (C and D) Contours of the pore P_0 and microjet morphologies. (E) Keyhole depths, d_1 and d_2 . Three time nodes are defined: At t_1 (magenta circle), with the keyhole closure, pore P_0 forms; at t_2 (green circle), the primary pore starts to rebound; and at t_3 (blue circle), the keyhole depth reaches a local minimum, and the pores start to migrate away from the keyhole. (F) Equivalent pore diameter, D_p ,

estimated from (C). (G) Distances of pores away from the nearest keyhole wall. (H) Formation of a NKB, attributed to the coupling between the existence of a protrusion and the rebound of pore P_1 . (I) Initial pore motions caused by the acoustic wave emitted from the NKB. L-V in (H) and (I) is the liquid-vapor interface of a keyhole or a pore. (J and K) X-ray images of keyhole pore collapse, rebound, and motion, corresponding to the two events indicated with the magenta and blue dashed rectangles in (E), respectively. All images were background corrected followed by contrast reversal. Frame-by-frame images are documented in movie S11 and fig. S8.

where there is a large thermal gradient field, and its motion is dominated by the competition between the thermocapillary and viscous drag forces. After the postulated phase explosion, pore P_2 , unlike pore P_1 , was not pushed away but “dances” with the keyhole bottom wall, until an abrupt morphology change of the keyhole bottom (because of the pressure drop inside) (fig. S18) successfully lures the pore in deep (Fig. 3G and fig. S17). The keyhole then grows rapidly owing to the increased laser absorption inside the forcedly developed bottom and eventually captures pore P_2 . The evolving distances of these two pores from the nearest keyhole wall (Fig. 3G) suggests two thresholds (plateaus in the plots) under this particular laser condition. One is the edge of the strong thermal gradient field, $42 \pm 2 \mu\text{m}$ from the keyhole wall, beyond which the thermocapillary force is negligible. The other is the point at which the two forces balance, $28 \pm 3 \mu\text{m}$, below which the thermocapillary force dominates because of the high thermal gradient of $\sim 10^8 \text{ K/m}$ (22) and draws the pore violently into the keyhole.

The thermocapillary-viscous drag force boundary remains nearly constant as the keyhole bottom evolves. When the keyhole drilling reaches its limit, the pore may become nearly stationary; for example, pore P_2 stops moving since time $18.40 \mu\text{s}$ for $\sim 8 \mu\text{s}$ (movie S11). The force balance could be then used to estimate the drag coefficient C_d (35, 36) [~ 6.0 in this case (22)], which has long been a controversial problem (35, 37). However, when the keyhole shrinks and expands, the pore dances along. The sharp and narrow thermocapillary-viscous drag force boundary implies that if the pore is around the boundary, it always manages to accommodate its motion to the local melt flow pattern. But if trapped inside, the pore is unable to escape because of the increasing attraction from the keyhole wall, as hinted at by the rapid decrease in the distance away from the nearest keyhole wall (Fig. 3G).

With operando high-speed synchrotron x-ray imaging, we found that the boundary between the keyhole porosity and stable melting regimes in the P - V space was unexpectedly smooth and sharp, varying only slightly with the presence of powder. Close to this porosity boundary, we discovered a new mechanism that is responsi-

ble for the formation of small and often spherical pores: Acoustic waves generated during the highly dynamic laser-metal interaction play a key role in driving pores near the keyhole tip far enough away from the large thermal gradient field around the keyhole that they are trapped through solidification. A more detailed investigation of the mechanisms of acoustic waves is merited. In addition to this dominant mechanism, at low power levels a secondary mechanism results in pore trapping as a fluctuating keyhole collapses and retracts; drag forces may also pull the pore away from the retracting keyhole. At a broader scale, not only does the existence of a well-defined keyhole porosity boundary offer a more secure basis for predicting process windows, but the new understanding of how small pores are generated close to the boundary explains some of the confusion in the LPBF literature about the origins of porosity. In other words, small spherical pores may be inherited from the powder, or they may originate from the use of marginally stable melting conditions.

REFERENCES AND NOTES

- S. A. Khairallah, A. T. Anderson, A. Rubenchik, W. E. King, *Acta Mater.* **108**, 36–45 (2016).
- W. J. Sames, F. List, S. Pannala, R. R. Dehoff, S. S. Babu, *Int. Mater. Rev.* **61**, 315–360 (2016).
- J. H. Martin *et al.*, *Nature* **549**, 365–369 (2017).
- R. Cunningham, S. P. Narra, C. Montgomery, J. Beuth, A. D. Rollett, *JOM* **69**, 479–484 (2017).
- T. DebRoy *et al.*, *Prog. Mater. Sci.* **92**, 112–224 (2018).
- R. Fabbro, *J. Phys. D Appl. Phys.* **43**, 445501 (2010).
- R. Cunningham *et al.*, *Science* **363**, 849–852 (2019).
- A. Kaplan, *J. Phys. D Appl. Phys.* **27**, 1805–1814 (1994).
- C. Zhao *et al.*, *Phys. Rev. X* **9**, 021052 (2019).
- W. E. King *et al.*, *J. Mater. Process. Technol.* **214**, 2915–2925 (2014).
- A. Matsunawa, J.-D. Kim, N. Seto, M. Mizutani, S. Katayama, *J. Laser Appl.* **10**, 247–254 (1998).
- N. Seto, S. Katayama, A. Matsunawa, *J. Laser Appl.* **12**, 245–250 (2000).
- A. A. Martin *et al.*, *Nat. Commun.* **10**, 1987 (2019).
- J. C. Ion, H. R. Shercliff, M. F. Ashby, *Acta Metall. Mater.* **40**, 1539–1551 (1992).
- J. L. Beuth *et al.*, in *Solid Freeform Fabrication Proceedings*, (Univ. Texas at Austin, 2013), pp. 655–665.
- H. Gong, K. Rafi, H. Gu, T. Starr, B. Stucker, *Additive Manufacturing* **1–4**, 87–98 (2014).
- C. Zhao *et al.*, *Sci. Rep.* **7**, 3602 (2017).
- N. D. Parab *et al.*, *J. Synchrotron Radiat.* **25**, 1467–1477 (2018).
- N. P. Calta *et al.*, *Rev. Sci. Instrum.* **89**, 055101 (2018).
- C. L. A. Leung *et al.*, *Nat. Commun.* **9**, 1355 (2018).
- A. A. Martin *et al.*, *Mat. Today Adv.* **1**, 100002 (2019).
- Materials and methods are available as supplementary materials.
- J. Y. Lee, S. H. Ko, D. F. Farson, C. D. Yoo, *J. Phys. D Appl. Phys.* **35**, 1570–1576 (2002).
- S. A. Khairallah *et al.*, *Science* **368**, 660–665 (2020).

- R. Fabbro *et al.*, *J. Laser Appl.* **30**, 032410 (2018).
- M. Bayat *et al.*, *Additive Manufacturing* **30**, 100835 (2019).
- J. Dear, J. Field, A. J. Walton, *Nature* **332**, 505–508 (1988).
- M. B. Lesser, J. E. Field, *Annu. Rev. Fluid Mech.* **15**, 97–122 (1983).
- G. N. Sankin, W. N. Simmons, S. L. Zhu, P. Zhong, *Phys. Rev. Lett.* **95**, 034501 (2005).
- S. Fujikawa, T. Akamatsu, *J. Fluid Mech.* **97**, 481–512 (2006).
- C. J. Todaro *et al.*, *Nat. Commun.* **11**, 142 (2020).
- A. Miotello, R. Kelly, *Appl. Phys., A Mater. Sci. Process.* **69**, S67–S73 (1999).
- P. Lorazo, L. J. Lewis, M. Meunier, *Phys. Rev. Lett.* **91**, 225502 (2003).
- J. C. Ramirez-San-Juan *et al.*, *Opt. Express* **18**, 8735–8742 (2010).
- T. Watanabe, Y. Kukita, *Phys. Fluids A Fluid Dyn.* **5**, 2682–2688 (1993).
- N. O. Young, J. S. Goldstein, M. J. Block, *J. Fluid Mech.* **6**, 350–356 (2006).
- J. Magnaudet, I. Eames, *Annu. Rev. Fluid Mech.* **32**, 659–708 (2000).

ACKNOWLEDGMENTS

This research used resources of the Advanced Photon Source, a U.S. Department of Energy (DOE) Office of Science User Facility operated for the DOE Office of Science by Argonne National Laboratory under contract DE-AC02-06CH11357. We acknowledge A. Deriy and F. D. Carlo at the APS and Z. Guo and W. Chen at Purdue University for their technical support of the beamline experiments. We also acknowledge R. Cunningham at Messer Americas, W. King at The Barnes Group Advisors, and D. Du at Tsinghua University for the fruitful discussions. C.Z., T.S., and N.D.P. thank Argonne National Laboratory for supporting efforts before their relocations on developing beamline capabilities and the operando laser system that eventually led to this work. C.Z. thanks D. Du, F. Lin, G. Liu, and X. Liu at Tsinghua University for the financial support and assistance during the coronavirus disease 2019 (COVID-19) crisis. **Funding:** The work was supported by the start-up fund from the Department of Mechanical Engineering at Tsinghua University, the start-up fund from the University of Virginia, the Department of Defense Office of Economic Adjustment under award ST1605-17-02, the National Aeronautics and Space Administration (NASA) University Leadership Initiative program under grant 80NSSC19M0123, and the National Science Foundation under grant 1752218. **Author contributions:** T.S., A.D.R., and C.Z. conceived the idea and designed the project. C.Z., T.S., and N.D.P. designed and performed the experiments with assistance from K.F. and A.D.R.; C.Z., T.S., K.F., and N.D.P. designed and built the LPBF simulator. C.Z. carried out the image processing and data analysis and interpretation and proposed and proved the acoustic wave mechanism, with help from all authors. W.T. and X.L. conducted simulations, with input from C.Z. The manuscript was written by C.Z., T.S., and A.D.R. All authors commented on the manuscript. **Competing interests:** The authors declare no competing interests. **Data and materials availability:** All data needed to evaluate our conclusions are provided in the manuscript or the supplementary materials.

SUPPLEMENTARY MATERIALS

science.sciencemag.org/content/370/6520/1080/suppl/DC1
Materials and Methods
Figs. S1 to S22
References (38–52)
Movies S1 to S12

4 June 2020; accepted 20 October 2020
10.1126/science.abd1587

Critical instability at moving keyhole tip generates porosity in laser melting

Cang Zhao, Niranjan D. Parab, Xuxiao Li, Kamel Fezzaa, Wenda Tan, Anthony D. Rollett and Tao Sun

Science **370** (6520), 1080-1086.
DOI: 10.1126/science.abd1587

Driving the pores away

The formation of "keyholes" (vapor-filled depressions) during additive manufacturing leads to porosity, which degrades alloy performance, especially fracture properties, and remains a big challenge for the 3D printing of metals. Zhao *et al.* used high-speed x-ray imaging to take a detailed look at how keyhole formation connects to porosity in a titanium alloy. They found that instability at the keyhole tip drives pores away to get trapped in the solidification front. Understanding this process and the operating parameters under which it occurs provides a roadmap for avoiding porosity and building high-quality metal parts.

Science, this issue p. 1080

ARTICLE TOOLS

<http://science.sciencemag.org/content/370/6520/1080>

SUPPLEMENTARY MATERIALS

<http://science.sciencemag.org/content/suppl/2020/11/23/370.6520.1080.DC1>

REFERENCES

This article cites 51 articles, 2 of which you can access for free
<http://science.sciencemag.org/content/370/6520/1080#BIBL>

PERMISSIONS

<http://www.sciencemag.org/help/reprints-and-permissions>

Use of this article is subject to the [Terms of Service](#)

Science (print ISSN 0036-8075; online ISSN 1095-9203) is published by the American Association for the Advancement of Science, 1200 New York Avenue NW, Washington, DC 20005. The title *Science* is a registered trademark of AAAS.

Copyright © 2020, American Association for the Advancement of Science